

## Full length article

## The influence of nanoparticles on dendritic grain growth in Mg alloys

Enyu Guo <sup>a, b, \*\*</sup>, Sansan Shuai <sup>c, d</sup>, Daniil Kazantsev <sup>b, e</sup>, Shyamprasad Karagadde <sup>f</sup>,  
A.B. Phillion <sup>g</sup>, Tao Jing <sup>d</sup>, Wenzhen Li <sup>d</sup>, Peter D. Lee <sup>b, e, \*</sup>

<sup>a</sup> Key Laboratory of Solidification Control and Digital Preparation Technology (Liaoning Province), School of Materials Science and Engineering, Dalian University of Technology, Dalian, 116024, China

<sup>b</sup> School of Materials, The University of Manchester, Manchester, M13 9PL, UK

<sup>c</sup> School of Materials Science and Engineering, Shanghai University, Shanghai, 200072, China

<sup>d</sup> School of Materials Science and Engineering, Tsinghua University, Beijing, 100084, China

<sup>e</sup> Research Complex at Harwell, RAL, Didcot, OX11 0FA, UK

<sup>f</sup> Department of Mechanical Engineering, Indian Institute of Technology Bombay, 400076, India

<sup>g</sup> Department of Materials Science and Engineering, McMaster University, Hamilton, L8S 4L7, Canada

## ARTICLE INFO

## Article history:

Received 14 November 2017

Received in revised form

4 April 2018

Accepted 11 April 2018

Available online 14 April 2018

## Keywords:

Metal matrix nanocomposites

Dendritic solidification

Nanoparticles

Tomography

Iterative image reconstruction

## ABSTRACT

Melt processing offers a cost effective method for producing metal matrix nanocomposite (MMNC) components; however, the influence of nanoparticles on the evolving microstructure during solidification is still not well understood. In this study, the effect of SiC nanoparticles on  $\alpha$ -Mg dendrite evolution in a Mg-25Zn-7Al (wt.%) alloy was investigated through 4D (three dimensions plus time) synchrotron tomographic quantification of solidification experiments conducted at different cooling rates with and without nanoparticles. Key features of the solidifying primary  $\alpha$ -Mg dendritic grains were quantified, including grain morphology, size distribution, and dendrite tip velocity. To obtain the high-contrast tomography dataset necessary for structure quantification, a new image reconstruction and processing methodology was implemented. The results reveal that the addition of nanoparticles increases grain nucleation whilst restricting dendritic growth and altering the dendritic grain growth morphology. Using LGK model calculations, it is shown that these changes in solidification microstructure occur as a result of nanoparticle-induced restriction in Zn's effective diffusivity ahead of the dendrite tips, reducing tip velocity. The results both suggest the key phenomena required to be simulated when numerically modelling solidifying Mg-based MMNC and provide the data required to validate those models.

© 2018 Acta Materialia Inc. Published by Elsevier Ltd. All rights reserved.

## 1. Introduction

Nanoparticle (NP) reinforced light metal alloys, commonly known as metal matrix nanocomposites (MMNCs), are gaining interest for transportation, aerospace and defense applications due to their low density and high specific strengths [1,2] relative to non-reinforced alloys. The strength enhancement results from the combination of precipitate strengthening and grain refinement, depending on the type of particles including SiC, Al<sub>2</sub>O<sub>3</sub>, TiB<sub>2</sub>, Y<sub>2</sub>O<sub>3</sub> and AlN [3–7]. MMNCs are of particular interest for near-net-shape

castings where the solidification microstructure plays a key role in determining the final microstructure and thus the in-service mechanical properties of components.

In recent years, great effort has been made to explore the influence of NPs on liquid metal processing, solidification microstructure and mechanical behaviour [1,2,8–13]. Observations of the post-solidified microstructure containing NPs revealed a much finer grain structure than their NP-free counterparts [9,11,14], suggesting a grain refinement effect. In one study, the size of Mg grains decreased from 110  $\mu$ m in the NP-free alloy to 30  $\mu$ m in samples containing 6 vol.% SiC NPs [14]. A second study showed that the dendritic growth was restricted when TiC<sub>0.7</sub>N<sub>0.3</sub> NPs were added to a Sn-Al alloy, leading to a finer microstructure [15]. Other interesting effects, such as the modification of the dendrite's surface via NPs, have also been documented [16]. These observations were supported by theoretical analyses, suggesting that densely packed NPs may block solute diffusion during solidification [17].

\* Corresponding author. School of Materials, The University of Manchester, Manchester, M13 9PL, UK.

\*\* Corresponding author. Key Laboratory of Solidification Control and Digital Preparation Technology (Liaoning Province), School of Materials Science and Engineering, Dalian University of Technology, Dalian, 116024, China.

E-mail addresses: [eyguo@dlut.edu.cn](mailto:eyguo@dlut.edu.cn) (E. Guo), [pdlee123@gmail.com](mailto:pdlee123@gmail.com) (P.D. Lee).

Furthermore, particles ahead of the solid/liquid interface might be pushed or engulfed, depending on many factors including the dendrite growth velocity, interfacial energy, particle size, and particle thermal properties [18–20].

*In situ* studies of the effect of particles on evolving dendritic structures, through direct experimental observation, are limited [16,21,22]. One early study [21] examined particle-interface interactions in a transparent organic system, showing that the particles influenced morphological transitions, such as dendritic-to-cellular, and caused dendrite tip splitting and hyper branching. Due to the advent of 3rd generation synchrotrons, time resolved studies of structural evolution in a wide range of metallic materials are now possible, through either 2D synchrotron X-ray radiography [23–27] or 3D synchrotron X-ray tomography [28–36]. Recently, the latter method has been used to investigate the effect of nanoparticles on solidification microstructure development in Al alloys to reveal dendrite growth mechanisms in fcc crystal structures in the presence of NPs [16,22]. Although 2D radiography provides faster imaging acquisition speed, time-lapse (3D + time) tomography provides better structural detail while still possessing reasonable temporal resolution. For some cases where the microstructure is very complex, such as hcp alloys [37–40], 3D tomography is required as the sample geometry for 2D radiography, being very thin, restricts growth.

In this work, the influence of SiC NPs on the nucleation and growth of  $\alpha$ -Mg dendrites during solidification is investigated in a Mg–Zn–Al alloy through fast time-lapse synchrotron X-ray tomography. The effect of NPs on the dendritic growth is examined for two different cooling rates, 3 and 12 °C/min. The difference in dendrite nucleation, growth, and morphology, is contrasted with and without NPs, to reveal the impact of NPs on the microstructure during solidification. It is noted that these experiments are designed to study the microstructural evolution under the influence of NPs, and not to directly observe the NPs themselves. Analytical modelling is then performed to develop appropriate theoretical ideas that explain the influence of NPs on dendritic growth in Mg alloys.

## 2. Materials and experimental methods

### 2.1. Sample preparation

Model magnesium alloys, Mg–25 wt.%–Zn–7wt.%Al (NP-free, or containing ~0.7 wt.% SiC NPs), were used in this study. The alloys were prepared by combining an AZ91D (Mg–9wt.%Al–0.5 wt.%Zn) (or AZ91D containing 1 wt.% SiC NP<sup>1</sup>) alloy and a Zn ingot (99.9%) in a steel crucible, and melted under argon gas protection. Zn was added to improve image contrast during synchrotron X-ray tomography [29]. Ultrasonic treatment was applied to the NP-containing alloy to break up any agglomerated NP clusters and homogenize the chemical composition. The ultrasonic treatment was not applied to the NP-free alloy. In both cases, the melt was then cast into a preheated mild steel mould [10]. Finally, small cylindrical samples of  $\phi \sim 1.2$  mm were machined from the casting for the synchrotron solidification experiments and encapsulated following the method described in Ref. [28].

### 2.2. Synchrotron solidification experiments

The *in situ* synchrotron X-ray tomography experiments were carried out at the Diamond–Manchester Beamline (I13-2) of the

Diamond Light Source (DLS, U.K.). During each experiment, the sample was heated up to ~30 °C above the liquidus temperature and held at that temperature for 20 min (10 min for the NP alloy in order to minimize NPs agglomeration). Then, the sample was solidified by applying a prescribed cooling rate. In total, 4 experiments were performed on 2 alloys (NP-free, NP) and at 2 cooling rates (3, 12 °C/min).

The tomography scans were recorded during solidification using a pink beam (energy range 15–30 keV) and an imaging system composed of a 4 × objective, a single crystal CdWO<sub>4</sub> scintillator, and a PCO Edge 5.5 CMOS camera that was binned to 1280 × 1080 pixels, resulting in 1.6  $\mu$ m/pixel. For each scan, 1200 projections were acquired, each at an exposure time of 12 ms, resulting in a scan time of 14.4 s. Note however, that the scan-to-scan cycle time was 36 s, due to a time delay needed for system re-initialization. The 36 s cycle time corresponds to 1.8 and 7.2 °C, respectively, for the cooling rates of 3 and 12 °C/min. Accordingly, the error in temperature for the features in each tomographic image is assumed to be the same value.

### 2.3. Tomographic image reconstruction and image processing methods

Due to noisy, underexposed projection data with artifacts, different reconstruction methods were tested. The collected tomographic data was initially reconstructed using a conventional Filtered Back Projection (FBP) algorithm. However, the reconstructed images obtained were of low contrast, noisy, and contained severe ring artefacts; therefore, they were not suitable for segmentation and quantification (Fig. 1 (a)). To overcome this restriction, a model-based iterative reconstruction (MBIR) algorithm was applied, based on the Group-Huber data misfit method. This reconstruction technique significantly improves segmentation while minimizing ring artefacts (Fig. 1 (b)) [41–43]. Additionally,

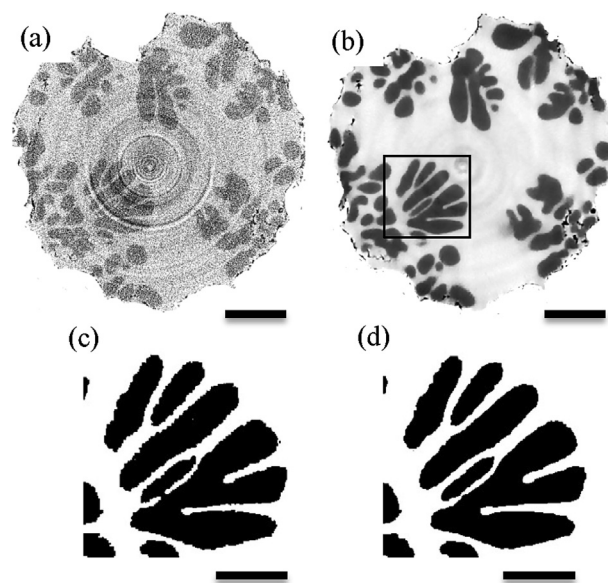


**Fig. 1.** A comparison of reconstructed images using (a) conventional FBP reconstruction, and (b) MBIR reconstruction. (c) and (d) are segmented dendrites, as enlarged images indicated by rectangle in (b), using (c) MBIR-TV algorithm, and (d) MBIR-TV-LT, respectively. Note in (b) light grey = liquid, dark grey = dendrite, black = pore. Note that much smoother and realistic contours of the segmented image in (d) using the MBIR-TV-LT method. Scale bar equals 300  $\mu$ m for (a) and (b), and 150  $\mu$ m for (c) and (d).

<sup>1</sup> The processing procedure creating the original AZ91D alloy containing SiC nanoparticles (average size: ~40 nm) is described in Ref. [9].

3D edge-preserving regularization was used to stabilise convergence and further improve the signal-to-noise ratio of the MBIR algorithm. The regularization consisted of two terms: total variation (TV) semi-norm and a higher-order Lysaker-Lundervold-Tai (LLT) penalty. The TV-related sub-problem was solved using the Split-Bregman algorithm and the LLT-related 4<sup>th</sup> order partial differential equation was minimized explicitly. The convex combination of two solutions was taken in order to achieve a piecewise-smooth reconstruction. Note that the piecewise-constant solution obtained using the TV-term alone is not suitable for this data. When using TV regularization alone, the reconstructed dendritic branches have unrealistic saw-shaped surfaces, Fig. 1 (c). In contrast, an averaged combination of TV and LLT penalties led to segmented data that are locally smooth and better fit the physical expectations of the data, Fig. 1 (d). The mathematical details of the implementation of this new reconstruction technique can be found in Ref. [43].

After the image reconstruction and pre-processing, the dendrites were segmented using a global threshold value. The data was cropped to a small volume and analysed using the ImageJ and Avizo® (Thermo Fisher Scientific, USA) software tools.

### 3. Results and discussion

#### 3.1. General microstructural observations

Fig. 2 shows a series of two-dimensional longitudinal slices at different temperatures for each of the four experiments. This series of images provides a general overview and comparison of the microstructural characteristics resulting from the addition of NPs as a function of cooling rate. (Note,  $T_l$  denotes the melt temperature immediately prior to the first nucleation of solid.) From this series of images, a number of salient observations can be made. First, the general size of  $\alpha$ -Mg grains in NP-free Mg-25Zn-7Al, Fig. 2(a–d) and Fig. 2(i–l), was larger than in NP Mg-25Zn-7Al, Fig. 2(e–h) and Fig. 2(m–p), for the same cooling rate. Thus, a significantly finer solidification microstructure was obtained through the addition of SiC NPs, indicating enhanced grain nucleation. Second, the faster cooling rate of 12 °C/min also led to a finer grain structure in both the NP-free and the NP alloys, Fig. 2(a–d) and Fig. 2(e–h), as compared to Fig. 2(i–l) and Fig. 2(m–p). Third, the shape of the NP-free grains appears to be dendritic, while the shape of the NP grains appears to be more globular. Finally, the  $\alpha$ -Mg dendrites appear to have nucleated heterogeneously, either on the oxide skin of the

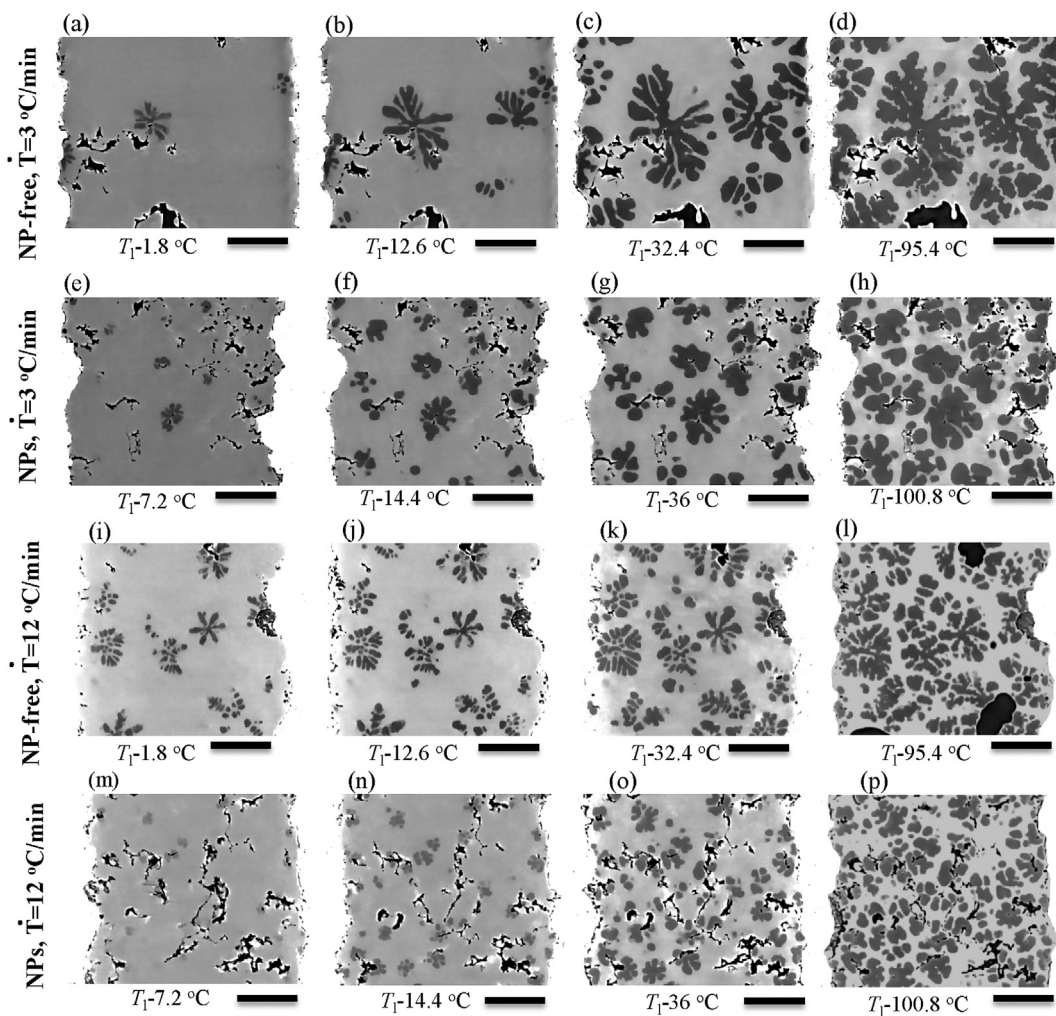


**Fig. 2.** Longitudinal slices showing the solidification dendritic structures of NP-free Mg-25Zn-7Al (a–d, i–l) and NP Mg-25Zn-7Al (e–h, m–p) alloys. Cooling rates were 3 °C/min for a–h, and 12 °C/min for i–p. The temperature is indicated below each figure. Scale bar in each figure is 300  $\mu$ m. Note that in the figure light grey = liquid, dark grey = dendrite, black = pore.



sample or on pre-existing pores (black regions in Fig. 2) within the melt (which most likely have an oxide at their surface). After nucleation, the dendrites that nucleated on the sample surface grew towards the centre because of the presence of a small thermal gradient between the “cooler” wall relative to the interior of the sample. However, the thermal gradient was not quantified. Dendrites that nucleated in the interior of the melt grew in all directions, forming very complex equiaxed branching structures. All of these details are examined further in 3D, below.

### 3.2. Nucleation mechanisms

Fig. 2 qualitatively suggests that more grains formed in the NP alloy than in the NP-free counterpart. However, 2D cross-sectional images can be misleading, especially in Mg alloys, where a hyper-branched dendrite can be cut multiple times by the cross-sectional plane; nucleation mechanisms are better examined in 3D. Fig. 3 shows the 3D evolution of dendrites during solidification for the NP-free and NP samples at the different cooling rates, as seen from the top of the cylinder. In these images, the dendrites were analysed from a small sub-volume ( $\varphi(1.1\text{--}1.2) \times 1.4\text{ mm}^3$ ) and individually colour-rendered. Examining first the image of NP-free Mg-25Zn-7Al cooled at  $3^\circ\text{C}/\text{min}$ , Fig. 3(a), it can be seen that 24 grains were initially observed to nucleate heterogeneously on the oxide skin of the sample wall, growing inwards. Upon further cooling of  $1.8^\circ\text{C}$ , Fig. 3(b), 14 more grains nucleated, including 4 grains completely within the interior of the sample. It appears that these 4 dendrites nucleated from the surface of pre-existing pores within the melt. Only 3 more dendrites nucleated after this time. In comparison, 109 grains in NP Mg-25Zn-7Al were observed in the first tomogram cooled at  $3^\circ\text{C}/\text{min}$  (Fig. 3(d)), and they nucleated both on the sample surface and within the melt. In the second tomogram, Fig. 3(e),  $1.8^\circ\text{C}$  lower in temperature, 148 additional grains were observed. Only another 10 grains nucleated with further progression in solidification.

At the faster cooling rate of  $12^\circ\text{C}/\text{min}$ , Fig. 3(g–i) and (j–l), similar phenomena were observed, i.e. more grains formed in NP than in NP-free alloy. Specifically, 48 grains were observed initially in the sample, while almost 300 grains were observed in NP Mg-25Zn-7Al. With a temperature reduction of  $7.2^\circ\text{C}$ , the number of grains increased to 136 and 814 for the NP-free and NP samples, respectively. The significantly larger number of grains as compared to the  $3^\circ\text{C}/\text{min}$  case is due to the faster cooling rate. Supplementary Fig. S1 directly identifies the nucleation location, i.e. on the sample surface or within the melt.

Each grain was further analysed to determine the location of the grain centre relative to pores/oxides within the sample. For the NP-free alloys, it appeared that the origin/centre of all grains was in contact with a pore or oxide. For the NP alloy,  $\sim 5\%$  of the grains nucleated directly in the liquid, without being in contact with a pore. This suggests the one nucleation mechanism is on oxides either in the melt or even more prevalently on the surface of pre-existing pores.

The solid fraction, as calculated from the tomograms, is given below each image in Fig. 3. There appears to be a discrepancy between the temperature and solid fraction in the faster cooling rate case, Fig. 3(g–l), as the calculated solid fraction value is not large enough for the given temperature below  $T_i$ , and in some cases is smaller than the corresponding value for the slower cooling rate change. This issue is attributed to a larger temperature error at the higher cooling rate, as one scan covers  $7.2^\circ\text{C}$ .

Fig. 4 quantifies the evolution in the distribution of the volume-averaged grain diameter from each tomogram given in Fig. 3. It is seen that the peak position for both the NP-free and NP samples shifts to the right as cooling progresses and the dendrites grow, as

expected. Differences between the NP-free and NP samples are also visible. Specifically, the peak frequency for the NP-free sample cooled at  $3^\circ\text{C}/\text{min}$  only increases slightly (red curve in Fig. 4(a)), and then stabilizes afterwards (black curve in Fig. 4(a)), whereas the curves for the NP alloy become much wider as solidification progresses, with an increased value at the peak. This suggests that growth may be restricted in the NP containing samples, allowing greater undercooling to be achieved in the remaining interdendritic liquid and activating more of the heterogeneous nuclei there.

The data shown in Fig. 4 was also used to quantify the overall volume-averaged equivalent diameter of the grains cooled at  $3^\circ\text{C}/\text{min}$  as a function of temperature below the melting point:  $78 \pm 21\text{ }\mu\text{m}$ ,  $109 \pm 24\text{ }\mu\text{m}$ , and  $184 \pm 31\text{ }\mu\text{m}$  for the NP-free sample, and  $50 \pm 7\text{ }\mu\text{m}$ ,  $61 \pm 14\text{ }\mu\text{m}$ , and  $93 \pm 26\text{ }\mu\text{m}$  for the NP sample, at the temperatures shown in Fig. 3(a–c) and Fig. 3(g–i), respectively. Similar trends were observed in Fig. 4(b), for the cooling rate of  $12^\circ\text{C}/\text{min}$ , i.e. the volume-averaged equivalent diameters of the grains are  $56 \pm 10\text{ }\mu\text{m}$ ,  $88 \pm 28\text{ }\mu\text{m}$ , and  $99 \pm 35\text{ }\mu\text{m}$  for the NP-free sample, and  $42 \pm 7\text{ }\mu\text{m}$ ,  $52 \pm 12\text{ }\mu\text{m}$ , and  $62 \pm 14\text{ }\mu\text{m}$  for the NP sample at the temperatures shown in Fig. 3(d–f) and Fig. 3(j–l), respectively. Thus, the average grain size is on the order of 50% smaller when NPs are added to Mg, for the same cooling conditions. The measured data presented in Fig. 4 agree well with the qualitative observations presented in Fig. 3. This reduction in grain size has been demonstrated to result in an improved mechanical properties, as reported by previous studies in similar Mg alloys [1]. For example, Jia et al. reported that when the average grain size in AZ91D alloy was decreased from  $\sim 152\text{ }\mu\text{m}$  to  $\sim 102\text{ }\mu\text{m}$  after adding 1 wt.% SiC nanoparticles, the yield strength was increased by  $\sim 100\%$  [9].

The results given in Figs. 2–4 clearly show that the presence of NPs has a strong influence on grain size, and hence grain nucleation and growth, irrespective of the cooling rate. In melt processing, NPs tend to agglomerate into large particle clusters with various sizes due to their high surface energy [18,22,44]. Greer et al. [45] suggested that heterogeneous grain nucleation is inversely proportional to particle size, hence it is possible that agglomerated NPs might be more effective nuclei; however, these NP clusters are probably not crystallographically aligned and hence the argument of Greer et al. may not be applicable to them. Although individual particles have been found at the centre of grains, strongly indicating that they act as effective nucleation sites [11], clusters were found to be pushed by the primary dendrites [22].

The above results suggest several possible hypotheses as to why the addition of NPs causes such a significant reduction in grain size:

1. NPs act as a direct heterogeneous nucleant, either individually or as clusters;
2. NPs increase the formation of secondary phases that act as nuclei (e.g. oxide or other phases); and/or
3. NPs reduce solute effective diffusivity in liquid and hence increase the solute growth restriction effect.

To support hypothesis 1, prior authors have demonstrated that SiC particles show a low lattice spacing registry of only 4% with respect to the primary-Mg phase on their close packed planes [46]. Recent studies in the Mg-Al [47–50], and Mg-Al-Zn [4,9,51] families have also demonstrated, via optical metallography, the efficacy of SiC containing master alloy for grain refinement. Unfortunately, we did not find any direct evidence, such as the observation of SiC within the centre of a grain, to prove this hypothesis; the observation of direct nucleation in the melt when NPs are added suggests the mechanism is possible, but is not a dominant factor (since only ca. 5% of the grains nucleated in this manner). Further, although clustering of grains occurs, and increases the effective size of the

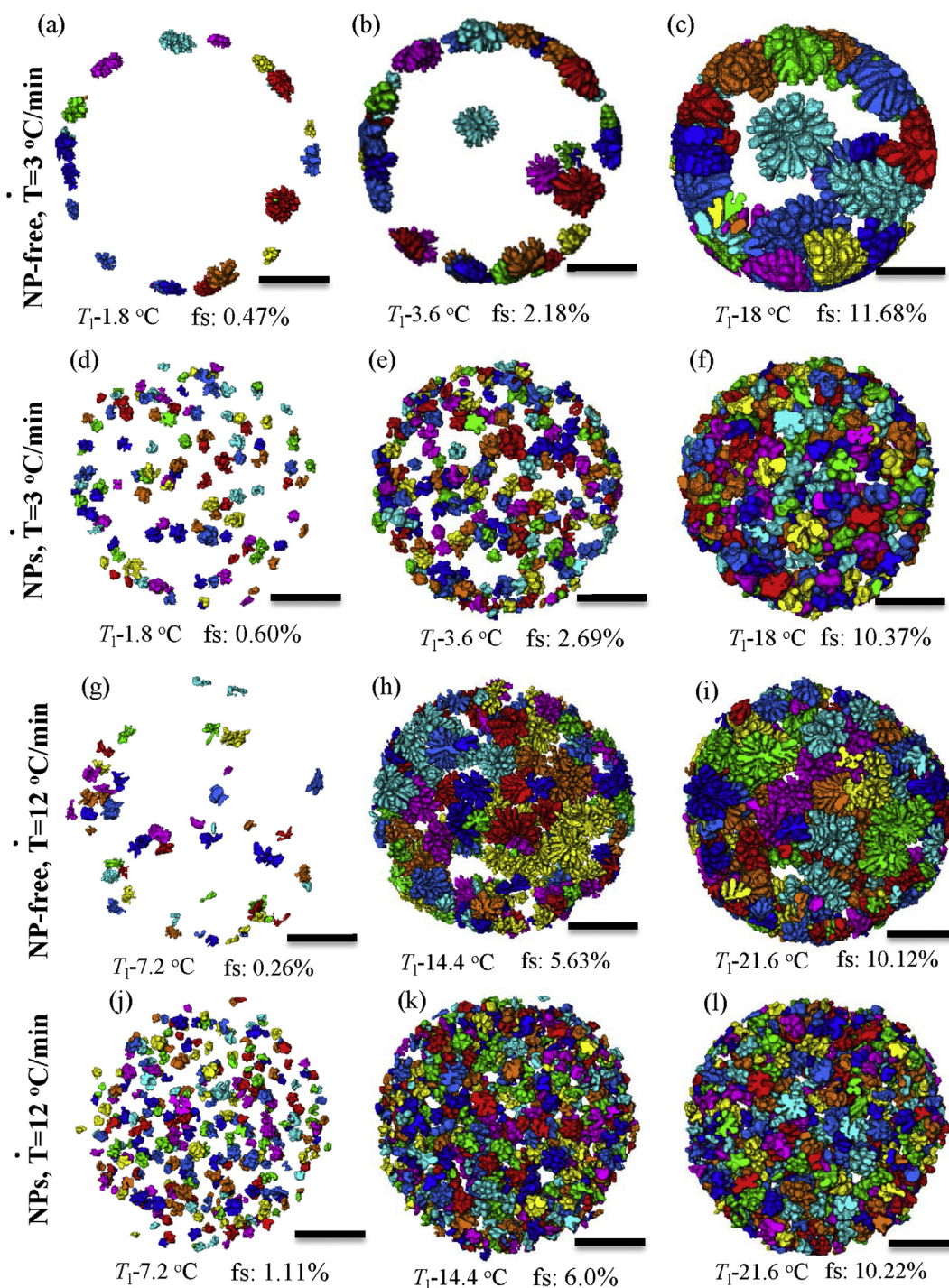


**Fig. 3.** Colour-rendered images showing the 3D grains of NP-free Mg-25Zn-7Al (a–c, g–i) and NP Mg-25Zn-7Al (d–f, j–l) during solidification at 3 °C/min (a–f) and 12 °C/min (g–l). Images were seen from top. Scale bar equals 300  $\mu$ m. The temperature and solid fraction ( $f_s$ ) are indicated below each figure. Note that the temperature variation for the indicated temperature is  $\sim 1.8$  and  $7.2$  °C for the cooling rate of 3 °C/min and 12 °C/min, respectively. (For interpretation of the references to colour in this figure legend, the reader is referred to the Web version of this article.)

potential nuclei, we would argue that the random crystallographic orientation of individual particles would reduce, rather than increasing a cluster's potency as a nucleus.

With regards to hypothesis 2, that NPs influence the formation of another phase that in turn acts as a nucleus, it has been proposed previously that SiC particles react with Al in Mg–Al melts to form  $\text{Al}_4\text{C}_3$ . These particles would also act as effective nucleants since

$\text{Al}_4\text{C}_3$  also has a low disregistry with Mg, 3.4%, and both form hexagonal crystal structures [52–54]. The formation of  $\text{Al}_4\text{C}_3$  is only possible when the melt is heated to a high temperature,  $\sim 150$  °C above the liquidus [47]. It is possible that this mechanism occurred in the NP alloy as the melt was heated to  $680$ – $700$  °C after ultrasonic treatment. Unfortunately, this hypothesis is very difficult to prove/disprove since (i)  $\text{Al}_4\text{C}_3$  is highly soluble in water and will

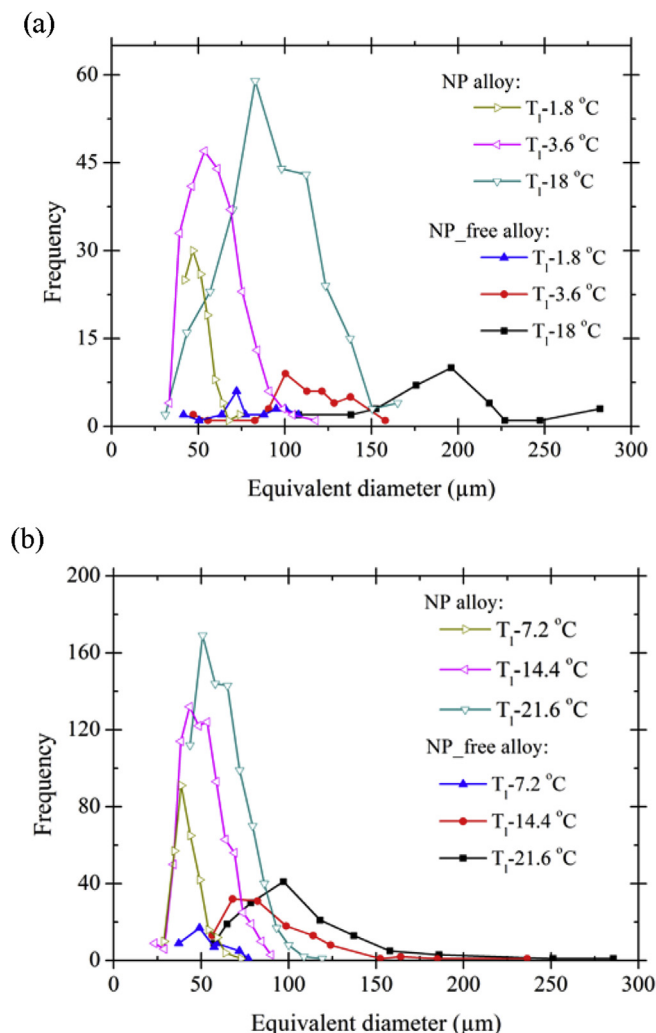


**Fig. 4.** Comparison of equivalent diameter distribution of grains in NP-free and NP Mg-25Zn-7Al alloys for different cooling conditions: (a) 3 °C/min; (b) 12 °C/min.

dissolve out of the matrix during sample preparation for metallography [49,50] and (ii) the small quantities that may form are not sufficient for detection via XRD.

Another potential secondary influence of NPs is that they help stabilise the formation oxides that act as a nucleant. We observed that in both the NP containing (95%) and in the NP free samples (100%) the grains appeared to grow from oxides either at the sample surface or on the surface of pre-existing pores. These pre-existing pores form during the *in situ* melting, and are then stabilized by the formation of oxides, e.g. MgO, that hold them in the melt. The number density and volume fraction of these pre-existing pores increased significantly with the addition of NPs. Further, EPMA compositional analysis of the NP and NP-free samples showed that the SiC content in the NP samples was higher on many of the pore surfaces as compared to the overall SiC content; this was not found on the pores of NP-free samples. MgO has been shown to be an effective nucleation site for Mg [12], as summarized in a review by St John et al. [6].

Therefore, our *in situ* observations directly support a refined hypothesis 2, that NPs cause more oxide to form, and that the oxide acts as a nucleation site. Additionally, the ultrasonic treatment (which was not applied to the NP-free alloy) may have increased the MgO oxide content within the melt as well.

Hypothesis 3 is that the presence of NPs in the melt acts as a barrier for diffusion of the solute causing growth restriction (Zn in this case), effectively increasing the growth restriction factor. This causes the grains to grow more slowly, and hence the remaining melt undercools to a greater extent, and hence more of the potential nuclei are activated. Since this is an indirect impact on nucleation, it is discussed in detail in section 3.4 and 3.5.

In summary, our results suggest that the influence of NP additions on grain size is most likely a result of several mechanisms, but we hypothesise that the dominant nucleation mechanism is the effect of NPs on increasing the amount of oxide in the melt. We will argue later that an equally important effect is the influence NPs have on growth restriction.

### 3.3. 3D dendritic morphology

Fig. 5 shows the evolution of four individual dendrites, one from each experiment, as a function of temperature. All images have the same scale bar except for the NP-free sample cooled at 3 °C/min, Fig. 5(a–d), due to its large size. By examining these images, one can observe the effect of NPs on grain morphology. First, the addition of NPs modifies the overall dendritic structure of Mg alloys. In the case of NP-free Mg-25Zn-7Al, the standard six-fold symmetric structure in the basal plane is observed. This is seen in both cooling rates, Fig. 5(b) and (j). However, both dendrites also contain more than 18 branches, suggesting that dendrite tip splitting is occurring. Similar six-fold structures were also observed in prior studies on Mg-25 wt.%Zn [29,37]. Second, the addition of SiC NPs causes the dendritic structure to be altered significantly, Fig. 5(e–h) and (m–p). In the NP Mg-25Zn-7Al alloy, most of the dendrites solidified at both cooling rates evolved towards a globular shape without obvious preference in growth direction. In fact, it was not possible to identify the six-fold crystal structure, and very few dendrites even possessed the fuzzy six-fold structure [29].

Recent studies have shown that dendrites in binary Mg–Zn alloys tend to change from a well-resolved six-fold hcp structure under low-to-moderate Zn content (e.g. Mg-25 wt.%Zn) to a hyper-branched structure with increased Zn content (e.g. Mg-38 wt.%Zn) [29,37,38], although the exact composition where the transition occurs remains unknown. The increased interfacial energy anisotropy caused by Zn is thought to be responsible for this phenomenon [37,55]. A similar morphological transition was observed in fcc Al due to increasing Zn content [55,56]. Based on the tomographic datasets acquired as part of this study, it is hypothesised that nanoparticles build up ahead of the solidification front, blocking Zn diffusion, and increasing the local Zn concentration. The increased Zn increases the interfacial energy anisotropy, altering the morphology from six-fold to a hyper-branched structure.

Another factor that may influence dendritic morphology is the grain spacing. When grains are close together, solute accumulation can begin very early in the growth process reducing the growth rate significantly and finally leading to globular morphologies. The average grain spacings are  $\sim 169 \mu\text{m}$  for the NP alloy and  $\sim 309 \mu\text{m}$  NP-free alloy at 3 °C/min, respectively, while they are  $\sim 122 \mu\text{m}$  and  $\sim 182 \mu\text{m}$  at 12 °C/min, respectively. The quantification suggests that the solute accumulation may begin earlier in the growth process for the NP alloys under the same cooling condition as compared to the NP-free condition, due to the larger grain density, reducing the growth rate and leading to the globular morphology. However, this cannot totally explain the large difference in morphology between the two alloys. For example, the dendritic grains in the NP alloy at 12 °C/min exhibit globular, while they are more dendritic in NP-free alloy at 3 °C/min even though the average grain space is similar.

However, it is not only Zn that alters solidification morphology. In previous research [15,16], inert NPs have also been known to



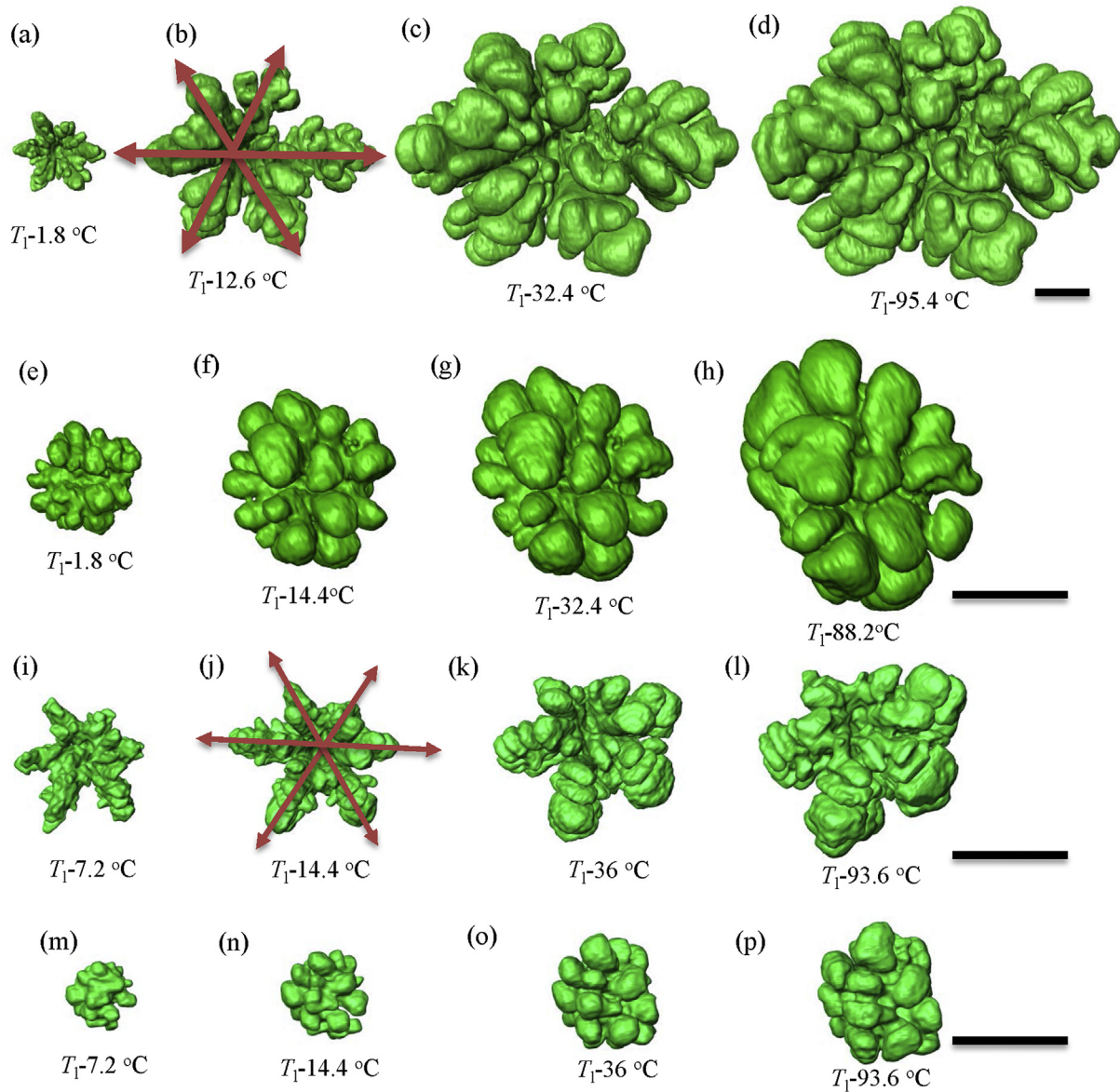


**Fig. 5.** Images showing the 3D dendritic evolution of NP-free (a–d, i–l) and NP Mg-25Zn-7Al (e–h, m–p) alloys. Cooling rates were 3 °C/min for a–h, and 12 °C/min for i–p. The temperature is indicated below each figure. Images in each horizontal panel share the same scale bar, and each scale bar equals 150  $\mu\text{m}$ . Note that the temperature uncertainty for the indicated temperature is 1.8 °C and 7.2 °C for the 3 °C/min and 12 °C/min cooling rate, respectively.

induce dendrite morphological modification of dendrites due to the addition of NPs. In the work by Daudin et al. [16] on a Al-Mg-Si alloy, a highly branched Al dendrite containing  $\text{Y}_2\text{O}_3$  NPs was reported after ultrasonic treatment of the melt, whereas the structure was less branched and coarser without ultrasonic treatment. The authors attributed this dendrite tip splitting to the large dispersion of NPs resulting from ultrasonic treatment. It is interesting to note that the cooling rate used by Daudin et al. was  $\sim 90\text{--}180\text{ }^\circ\text{C/min}$ , which is much faster than the experiments done in this study and may have resulted in increased particle engulfment rather than particle pushing.

In order to quantify the difference in morphology between the dendrites in each experiment, the grain solidity was analysed. Solidity is defined as the ratio of dendrite volume to the volume of a convex hull envelope containing it. The solidity can be used to

determine the compactness of a structure; a higher value means that a structure achieves a higher level of compactness. The values of solidity as a function of solidification temperature are plotted in Fig. 6. A number of observations can be made. First, solidity increases upon cooling, meaning that a more compact structure is formed as dendrites grow. It can be seen that the increase in solidity is greater at the lower cooling rate of 3 °C/min as compared to 12 °C/min. Second, the grain solidity in the NP samples is larger than in the NP-free alloy, suggesting that the dendritic structure is more compact in Mg alloys containing NPs. This quantification is consistent with the observations in Fig. 5(e–h) and (m–p) that dendrites in the NP samples appear to be more globular in structure. Third, the largest change in solidity was observed in NP-free sample cooled at 3 °C/min. This is likely to be caused by the dendrite coarsening that accompanies dendritic growth [33]. As

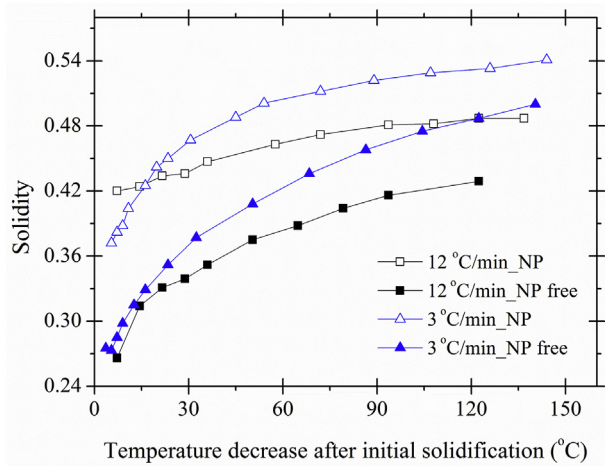


Fig. 6. Evolution of solidity for each typical grain in different compositions and cooling conditions.

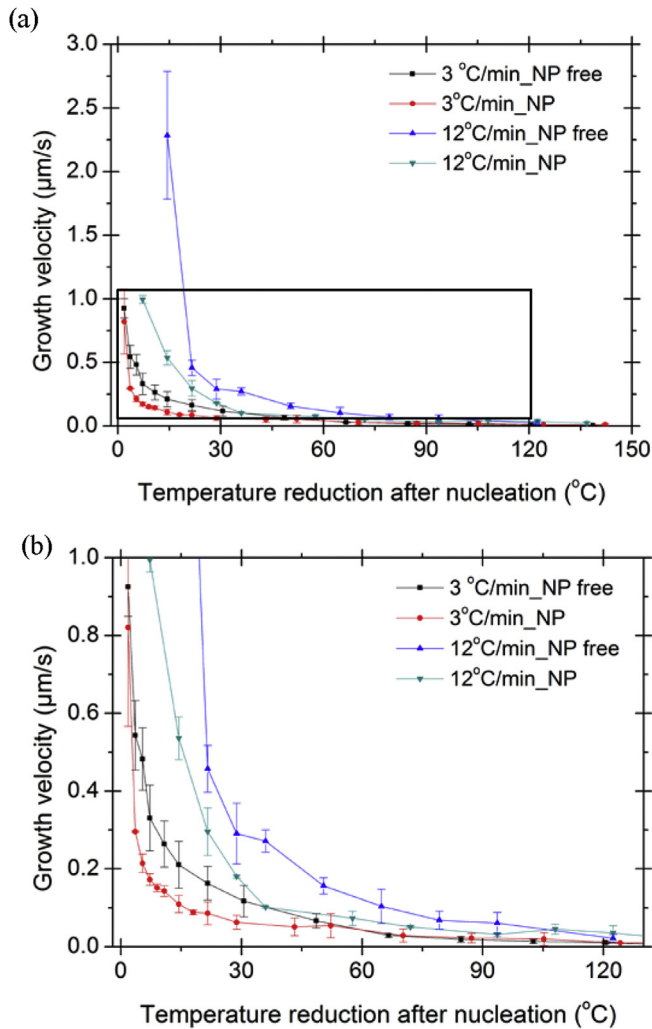


Fig. 7. Quantified dendrite tip velocity of each typical grain in different composition and cooling conditions. (b) Enlarged region as indicated by rectangle in (a).

coarsening is a solute-controlled diffusion phenomenon [57], a lower cooling rate and thus a longer diffusion time will increase coarsening.

#### 3.4. Calculation of dendrite tip growth velocity from tomographic datasets

The qualitative observations in Figs. 2 and 5 suggest that the growth velocity of dendrites is different under different compositions and cooling conditions. This is further elucidated through analysis of the dendrite tip velocity. The results are shown in Fig. 7 (additional results are given in Supplementary Fig. S2). Note that a few branches were measured for each dendrite. It is seen that the dendrites initially grew quickly under an unconstrained growth mode where the solute fields were not interacting with the surrounding dendrites. Then, growth slowed down gradually because of constraints imposed by solutal interactions with other dendrites in front of the evolving solid/liquid interface. Similar changes in growth rate over time were found in Al-Si alloys by Prasad et al. [58]. Note, Zn will dominate the growth restriction coefficient of the alloy due to its high content. Once physical impingement occurred, both dendrites stopped growing. It is further seen that the dendritic tip velocity in each NP sample was lower than in the corresponding NP-free sample for the same cooling rate. Finally, analysis of different branches of the same dendrite shows that the velocity of branches varied from one to the other, depending on the spatial position of the branch relative to the other surrounding dendrites. Note that the initial growth velocity measured in this study represents a lower bound, as the scan time was too slow to capture the fast initial transients.

It is well known that NPs will be either engulfed by the solidifying dendrites or pushed further into the liquid melt [20], depending on the growth speed of the solid phase. For NP having size of ~40 nm, this critical velocity is estimated to be ~100 μm/s [20]. As the cooling rate in this study and thus the solid growth velocity (<10 μm/s) are relatively low, it is expected that some of the SiC NPs and their clusters were pushed towards the liquid melt. As the local concentration of NPs increases, they would form a physical barrier, slowing the diffusion of the key solute element, which is Zn for this alloy [17,59]. NPs also increase the viscosity of the liquid melt, which, together with the physical blocking effect, reduces the effective diffusivity of both Al and Zn. This, in turn, restricts grain growth. EPMA analysis was performed on the as cast and *in situ* samples, indicating that a significant amount of Si (and hence SiC) was removed from the bulk alloy during *in situ* remelting (with some forming oxide as discussed above); hence the level of Si was too low to make any conclusions on the amount of SiC pushed by the primary phase during solidification.

A schematic is provided in Fig. 8 to demonstrate our hypothesised impact of NPs on dendritic growth. As can be seen, the density of NPs ahead of the solidification front increases because of particle pushing, reducing the diffusion length of solute, and thus reducing the effective solutal diffusivity. Other proposed mechanisms [15] for reduced dendritic growth velocity resulting from NP addition include a reduction in latent heat removal due to the low thermal conductivity of SiC NPs, growth front pinning by NPs through the Gibbs-Thomson effect, and an increase in the free energy of the growth phase by NP capture. However, the combined observations of reduced dendrite tip velocity (Fig. 7) and change to a hyper-branch morphology when NPs are added, strongly support the theory that in Mg alloys, NPs modify dendrite morphology by reducing the effective diffusivity of solute elements. This is the only mechanism that explains both observations.

#### 3.5. Calculation of dendrite tip growth velocity using the LGK analytical model

The LGK (Lipton-Glicksman-Kurz) analytical model predicts the dendritic growth velocity for free growth in undercooled melts. In



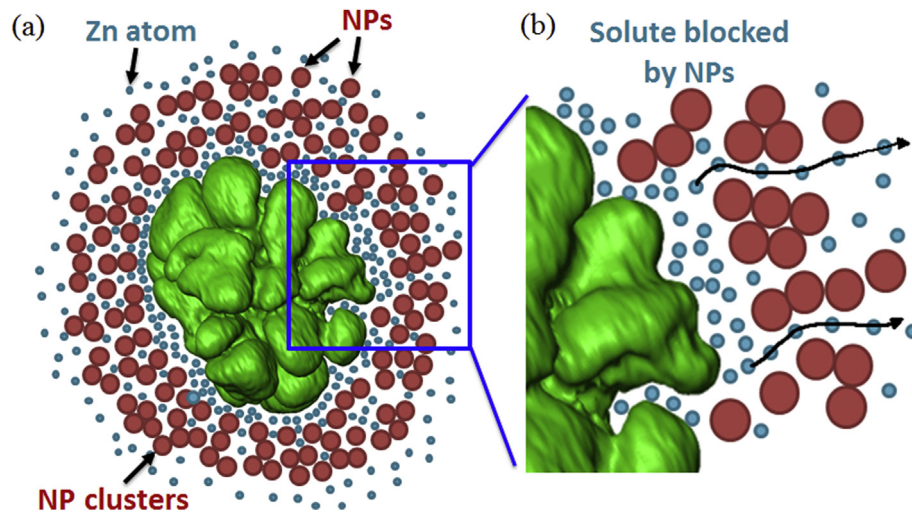


**Fig. 8.** (a) Schematic showing mechanism of the influence of nanoparticles/nanoparticle clusters on the dendritic growth; and (b) enlarged region illustrating how the Zn atom diffusion path lengths are increased by the high concentration of NPs at the solid-liquid interface.

this research, this model is applied to examine the influence of nanoparticles on the growth of  $\alpha$ -Mg dendrites, approximating the system as a Mg-25 wt.%Zn binary alloy. A summary of the model implementation is presented in the [supplementary Appendix 1](#). First, by iteratively solving equation (A1-A3) with the material properties provided in [supplementary Table S1](#), the initial tip velocity for the NP-free alloy was determined. The values given in [Table 1](#) show that the tip growth velocity agrees reasonably well with the initial growth velocities observed in the NP-free experiments performed at a cooling rate of 12 °C/min. Second, the same equations were used to determine the effective diffusivity that resulted in the analytically-calculated dendrite growth velocity matching the observed ones in the NP case [60]. This resulted in a reduction in the effective diffusivity value by about one-third as compared to the diffusivity for the NP-free alloy. This clearly supports the hypothesis that adding NPs impacts dendritic growth by modifying the effective solutal diffusivity ahead of the solid/liquid interface.

#### 4. Conclusions

*In situ* 4D synchrotron imaging was performed to investigate the influence of SiC NPs on grain nucleation and dendritic growth in a Mg-25 wt.%Zn-7 wt.%Al alloy. Analysis of the X-ray tomography datasets revealed that NP additions significantly reduce the grain size. Several potential mechanisms are hypothesised, and our observations suggest that SiC nanoparticles reduce grain size through two key mechanisms: 1. they increase the quantity of oxide heterogeneous nuclei; and 2. NPs reduce the effective diffusivity of Zn in the liquid, acting as an effective growth restrictor. In terms of heterogeneous nuclei, for samples with and without NPs, the vast majority of grains were observed to nucleate from oxide surfaces, both on the sample surface and from pre-existing pores stabilized

by the oxide in the melt. The addition of NPs, together with application of ultrasonic treatment, increased the number density and volume fraction of pre-existing pores, significantly increasing the oxide heterogeneous nucleation site density. Si content was concentrated on the surface of the pre-existing pores in the NP containing sample, suggesting SiC NPs migrated to the pore-liquid interface and stabilise the pores.

It was also found that NP additions modify the dendritic growth morphology, changing the structures from dendritic to hyper-branched with many split tips and a higher solidity as compared to NP-free grains.

Quantification of the dendrite tip growth velocities from the X-ray tomographic datasets in combination with analytical calculations using the LGK model revealed that the change in dendritic growth morphology results from the fact that NPs reduce the effective solutal diffusivity within the liquid ahead of the solid/liquid interface. This restricts redistribution of solute elements, increasing their concentration at the dendrite tips and finally leading to the hyper-branched grain morphology.

These results demonstrate the impact of fast 4D imaging in informing our understanding of the mechanisms present when processing MMNCs. Because the results are time resolved, they also provide outstanding data for validating computational simulations of microstructural evolution.

#### Data statement

Representative samples of the research data are given in the figures and supplementary data. Other datasets generated and/or analysed during this study are not publicly available due to their large size but are available from the corresponding authors on reasonable request.

**Table 1**  
Comparison of tip velocity between experimental measurements and LGK model predictions (cooling rate: 12 °C/min).

Alloy composition	Experimental measurement ( $\mu\text{m/s}$ )	LGK model ( $\mu\text{m/s}$ )	Effective diffusivity of Zn ( $\text{m}^2/\text{s}$ )
NP-Free	2.3	2.59	$1 \times 10^{-9}$
With 0.7 wt.%NP	0.7	0.71	$3 \times 10^{-10}$

## Acknowledgements

The work was funded in part by the European Commission (ExoMet Project, 7th Framework Programme, contract FP7-NMP3-LA-2012-280421), the EPSRC (EP/I02249X/1, EP/K007734/1, and EP/M009688/1) and National Natural Science Foundation of China (Grant No. 51690162). We acknowledge Diamond Light Source for providing the beamtime (MT11837-1), staff at I13 beamline for technical assistance and group members (especially Wenwu Xu, Biao Cai, Guang Zeng and Alex Leung) for beamline experiment support, and the use of facilities provided by the Research Complex at Harwell. Thanks to Dr. Hajo Dieringa of Helmholtz-Zentrum Geesthacht for assistance in sample preparation.

## Appendix A. Supplementary data

Supplementary data related to this article can be found at <https://doi.org/10.1016/j.actamat.2018.04.023>.

## References

- [1] H. Dieringa, Properties of magnesium alloys reinforced with nanoparticles and carbon nanotubes: a review, *J. Mater. Sci.* 46 (2) (2011) 289–306.
- [2] W.H. Sillekens, D.J. Jarvis, A. Vorozhtsov, V. Bojarevics, C.F. Badini, M. Pavese, S. Terzi, L. Salvo, L. Katsarou, H. Dieringa, The ExoMet project: EU/ESA research on high-performance light-metal alloys and nanocomposites, *Metall. Mater. Trans. A* 45A (8) (2014) 3349–3361.
- [3] A. Mortensen, J. Llorca, Metal matrix composites, *Annu. Rev. Mater. Res.* 40 (2010) 243–270.
- [4] J. Lelito, P.L. Zak, A.A. Shirzadi, A.L. Greer, W.K. Krajewski, J.S. Suchy, K. Haberl, P. Schumacher, Effect of SiC reinforcement particles on the grain density in a magnesium-based metal-matrix composite: modelling and experiment, *Acta Mater.* 60 (6–7) (2012) 2950–2958.
- [5] N. Chawla, K.K. Chawla, Metal Matrix Composites, second ed., Springer, New York, 2013.
- [6] D.H. Stjohn, M.A. Easton, M. Qian, J.A. Taylor, Grain refinement of magnesium alloys: a review of recent research, theoretical developments, and their application, *Metall. Mater. Trans. A* 44A (7) (2013) 2935–2949.
- [7] N. Chawla, Y.L. Shen, Mechanical behavior of particle reinforced metal matrix composites, *Adv. Eng. Mater.* 3 (6) (2001) 357–370.
- [8] B.F. Schultz, J.B. Ferguson, P.K. Rohatgi, Microstructure and hardness of Al<sub>2</sub>O<sub>3</sub> nanoparticle reinforced Al-Mg composites fabricated by reactive wetting and stir mixing, *Mater. Sci. Eng. A* 530 (2011) 87–97.
- [9] X.Y. Jia, S.Y. Liu, F.P. Gao, Q.Y. Zhang, W.Z. Li, Magnesium matrix nanocomposites fabricated by ultrasonic assisted casting, *Int. J. Cast Metal Res.* 22 (1–4) (2009) 196–199.
- [10] L. Katsarou, M. Mounib, W. Lefebvre, S. Vorozhtsov, M. Pavese, C. Badini, J.M. Molina-Aldareguia, C.C. Jimenez, M.T.P. Prado, H. Dieringa, Microstructure, mechanical properties and creep of magnesium alloy Elektron21 reinforced with AlN nanoparticles by ultrasound-assisted stirring, *Mater. Sci. Eng. A* 659 (2016) 84–92.
- [11] D.K. Wang, M.P. De Cicco, X.C. Li, Using diluted master nanocomposites to achieve grain refinement and mechanical property enhancement in as-cast Al-9Mg, *Mater. Sci. Eng. A* 532 (2012) 396–400.
- [12] H. Men, B. Jiang, Z. Fan, Mechanisms of grain refinement by intensive shearing of AZ91 alloy melt, *Acta Mater.* 58 (19) (2010) 6526–6534.
- [13] W. Mirihanage, W.W. Xu, J. Tamayo-Arizona, D. Eskin, M. Garcia-Fernandez, P. Srirangam, P. Lee, Synchrotron radiographic studies of ultrasonic melt processing of metal matrix nano composites, *Mater. Lett.* 164 (2016) 484–487.
- [14] L.Y. Chen, J.Y. Peng, J.Q. Xu, H. Choi, X.C. Li, Achieving uniform distribution and dispersion of a high percentage of nanoparticles in metal matrix nanocomposites by solidification processing, *Scripta Mater.* 69 (8) (2013) 634–637.
- [15] L.Y. Chen, J.Q. Xu, X.C. Li, Controlling phase growth during solidification by nanoparticles, *Mater. Res. Lett.* 3 (1) (2015) 43–49.
- [16] R. Daudin, S. Terzi, P. Lhuissier, J. Tamayo, M. Scheel, N. Hari Babu, D.G. Eskin, L. Salvo, Particle-induced morphological modification of Al alloy equiaxed dendrites revealed by sub-second in situ microtomography, *Acta Mater.* 125 (2017) 303–310.
- [17] L.Y. Chen, J.Q. Xu, H. Choi, H. Konishi, S. Jin, X.C. Li, Rapid control of phase growth by nanoparticles, *Nat. Commun.* 5 (2014) 3879.
- [18] X.H. Chen, H. Yan, Solid-liquid interface dynamics during solidification of Al 7075-Al<sub>2</sub>O<sub>3</sub>np based metal matrix composites, *Mater. Des.* 94 (2016) 148–158.
- [19] G. Wilde, M. Byrnes, J.H. Perepezko, Particle-dendrite interaction during undercooled liquid solidification of metal matrix composites, *J. Non-Cryst. Solids* 250–252 (1999) 626–631.
- [20] J.Q. Xu, L.Y. Chen, H. Choi, X.C. Li, Theoretical study and pathways for nanoparticle capture during solidification of metal melt, *J. Phys-Condens. Mat.* 24 (25) (2012).
- [21] J.A. Sekhar, R. Trivedi, Solidification microstructure evolution in the presence of inert particles, *Mater. Sci. Eng. A* 147 (1) (1991) 9–21.
- [22] R. Daudin, S. Terzi, P. Lhuissier, L. Salvo, E. Boller, Remelting and solidification of a 6082 Al alloy containing submicron yttria particles: 4D experimental study by in situ X-ray microtomography, *Mater. Des.* 87 (2015) 313–317.
- [23] A.G. Murphy, W.U. Mirihanage, D.J. Browne, R.H. Mathiesen, Equiaxed dendritic solidification and grain refiner potency characterised through in situ X-radiography, *Acta Mater.* 95 (2015) 83–89.
- [24] E. Liotti, A. Lui, R. Vincent, S. Kumar, Z. Guo, T. Connolly, I.P. Dolbnya, M. Hart, L. Arnberg, R.H. Mathiesen, P.S. Grant, A synchrotron X-ray radiography study of dendrite fragmentation induced by a pulsed electromagnetic field in an Al-15Cu alloy, *Acta Mater.* 70 (2014) 228–239.
- [25] T.M. Wang, J. Zhu, H.J. Kang, Z.N. Chen, Y.N. Fu, W.X. Huang, T.Q. Xiao, In situ synchrotron X-ray imaging on morphological evolution of dendrites in Sn-Bi hypoeutectic alloy under electric currents, *Appl. Phys. A* 117 (3) (2014) 1059–1066.
- [26] Y. Chen, B. Billia, D.Z. Li, H. Nguyen-Thi, N.M. Xiao, A.A. Bogno, Tip-splitting instability and transition to seaweed growth during alloy solidification in anisotropically preferred growth direction, *Acta Mater.* 66 (2014) 219–231.
- [27] A. Bogno, H. Nguyen-Thi, G. Reinhart, B. Billia, J. Baruchel, Growth and interaction of dendritic equiaxed grains: in situ characterization by synchrotron X-ray radiography, *Acta Mater.* 61 (4) (2013) 1303–1315.
- [28] S.S. Shuai, E.Y. Guo, A.B. Phillion, M.D. Callaghan, T. Jing, P.D. Lee, Fast synchrotron X-ray tomographic quantification of dendrite evolution during the solidification of Mg-Sn alloys, *Acta Mater.* 118 (2016) 260–269.
- [29] E.Y. Guo, A.B. Phillion, B. Cai, S.S. Shuai, D. Kazantsev, T. Jing, P.D. Lee, Dendritic evolution during coarsening of Mg-Zn alloys via 4D synchrotron tomography, *Acta Mater.* 123 (2017) 373–382.
- [30] M.A. Azeem, P.D. Lee, A.B. Phillion, S. Karagadde, P. Rocketta, R.C. Atwood, L. Courtois, K.M. Rahman, D. Dye, Revealing dendritic pattern formation in Ni, Fe and Co alloys using synchrotron tomography, *Acta Mater.* 128 (2017) 241–248.
- [31] B. Cai, J. Wang, A. Kao, K. Pericleous, A.B. Phillion, R.C. Atwood, P.D. Lee, 4D synchrotron X-ray tomographic quantification of the transition from cellular to dendrite growth during directional solidification, *Acta Mater.* 117 (2016) 160–169.
- [32] J.W. Gibbs, K.A. Mohan, E.B. Gulsoy, A.J. Shahani, X. Xiao, C.A. Bouman, M. De Graef, P.W. Voorhees, The three-dimensional morphology of growing dendrites, *Sci. Rep.* 5 (2015).
- [33] N. Limodin, L. Salvo, E. Boller, M. Suery, M. Felberbaum, S. Gailliege, K. Madi, In situ and real-time 3-D microtomography investigation of dendritic solidification in an Al-10 wt.% Cu alloy, *Acta Mater.* 57 (7) (2009) 2300–2310.
- [34] C. Punccebut, A.B. Phillion, J.L. Fife, P.D. Lee, Coupling in situ synchrotron X-ray tomographic microscopy and numerical simulation to quantify the influence of intermetallic formation on permeability in aluminium-silicon-copper alloys, *Acta Mater.* 64 (2014) 316–325.
- [35] S. Karagadde, P.D. Lee, B. Cai, J.L. Fife, M.A. Azeem, K.M. Kareh, C. Punccebut, D. Tsivoulas, T. Connolly, R.C. Atwood, Transgranular liquation cracking of grains in the semi-solid state, *Nat. Commun.* 6 (2015) 8300.
- [36] K.M. Kareh, P.D. Lee, R.C. Atwood, T. Connolly, C.M. Gourlay, Revealing the micromechanisms behind semi-solid metal deformation with time-resolved X-ray tomography, *Nat. Commun.* 5 (2014) 4464.
- [37] M.H. Yang, S.M. Xiong, Z.P. Guo, Effect of different solute additions on dendrite morphology and orientation selection in cast binary magnesium alloys, *Acta Mater.* 112 (2016) 261–272.
- [38] S.S. Shuai, E.Y. Guo, Q.W. Zheng, M.Y. Wang, T. Jing, Y.N. Fu, Three-dimensional  $\alpha$ -Mg dendritic morphology and branching structure transition in Mg-Zn alloys, *Mater. Charact.* 118 (2016) 304–308.
- [39] S.S. Shuai, E.Y. Guo, M.Y. Wang, M.D. Callaghan, T. Jing, Q.W. Zheng, P.D. Lee, Anomalous  $\alpha$ -Mg dendrite growth during directional solidification of a Mg-Zn alloy, *Metall. Mater. Trans. A* 47A (9) (2016) 4368–4373.
- [40] S.S. Shuai, E.Y. Guo, Q.W. Zheng, M.Y. Wang, T. Jing, Characterisation of three-dimensional dendritic morphology and orientation selection of  $\alpha$ -Mg in Mg-Ca alloy using synchrotron X-ray tomography, *Mater. Charact.* 111 (2016) 170–176.
- [41] P. Paleo, A. Mirone, Ring artifacts correction in compressed sensing tomographic reconstruction, *J. Synchrotron Radiat.* 22 (2015) 1268–1278.
- [42] D. Kazantsev, F. Bleichrodt, T.V. Leeuwen, A. Kaestner, P.J. Withers, K.J. Batenburg, P.D. Lee, A novel tomographic reconstruction method based on the robust Student's t function for suppressing data outliers, *IEEE Trans. Comp. Imaging* 3 (4) (2017) 682–693.
- [43] D. Kazantsev, E.Y. Guo, A.B. Phillion, P.J. Withers, P.D. Lee, Model-based iterative reconstruction using higher-order regularization of dynamic synchrotron data, *Meas. Sci. Technol.* 28 (9) (2017) 094004.
- [44] G. Cao, H. Konishi, X. Li, Mechanical properties and microstructure of SiC-reinforced Mg-(2,4)Al-1Si nanocomposites fabricated by ultrasonic cavitation based solidification processing, *Mater. Sci. Eng. A* 486 (1–2) (2008) 357–362.
- [45] A.L. Greer, A.M. Bunn, A. Tronche, P.V. Evans, D.J. Bristow, Modelling of inoculation of metallic melts: application to grain refinement of aluminium by Al-Ti-B, *Acta Mater.* 48 (11) (2000) 2823–2835.
- [46] A. Luo, Heterogeneous nucleation and grain refinement in cast Mg(AZ91)/SiCp metal matrix composites, *Can. Metall. Quart.* 35 (4) (1996) 375–383.

- [47] M.C. Gui, J.M. Han, P.Y. Li, Microstructure and mechanical properties of Mg-A19Zn/SiCp composite produced by vacuum stir casting process, *Mater. Sci. Technol.* 20 (6) (2004) 765–771.
- [48] Y.H. Liu, X.F. Liu, X.F. Bian, Grain refinement of Mg-Al alloys with Al<sub>4</sub>C<sub>3</sub>-SiC/Al master alloy, *Mater. Lett.* 58 (7–8) (2004) 1282–1287.
- [49] L. Lu, A.K. Dahle, D.H. StJohn, Heterogeneous nucleation of Mg-Al alloys, *Scripta Mater.* 54 (12) (2006) 2197–2201.
- [50] M.A. Easton, A. Schiffl, J.Y. Yao, H. Kaufmann, Grain refinement of Mg-Al(-Mn) alloys by SiC additions, *Scripta Mater.* 55 (4) (2006) 379–382.
- [51] R. Gunther, C. Hartig, R. Bormann, Grain refinement of AZ31 by (SiC)p: theoretical calculation and experiment, *Acta Mater.* 54 (20) (2006) 5591–5597.
- [52] L. Lu, A.K. Dahle, D.H. StJohn, Grain refinement efficiency and mechanism of aluminium carbide in Mg-Al alloys, *Scripta Mater.* 53 (5) (2005) 517–522.
- [53] M.X. Zhang, P.M. Kelly, M. Qian, J.A. Taylor, Crystallography of grain refinement in Mg-Al based alloys, *Acta Mater.* 53 (11) (2005) 3261–3270.
- [54] S. Zhang, W. Li, K. Yu, The grain refinement processes of magnesium alloys, *Foundry* 7 (2001) 373–375.
- [55] T. Haxhimali, A. Karma, F. Gonzales, M. Rappaz, Orientation selection in dendritic evolution, *Nat. Mater.* 5 (8) (2006) 660–664.
- [56] J. Friedli, J.L. Fife, P. Di Napoli, M. Rappaz, Dendritic growth morphologies in Al-Zn Alloys-Part I: X-ray tomographic microscopy, *Metall. Mater. Trans. A* 44A (12) (2013) 5522–5531.
- [57] P.W. Voorhees, Ostwald Ripening of two-phase mixtures, *Annu. Rev. Mater. Res.* 22 (1992) 197–215.
- [58] A. Prasad, S.D. McDonald, H. Yasuda, K. Nogita, D.H. StJohn, A real-time synchrotron X-ray study of primary phase nucleation and formation in hypoeutectic Al-Si alloys, *J. Cryst. Growth* 430 (2015) 122–137.
- [59] K. Wang, H.Y. Jiang, Y.W. Jia, H. Zhou, Q.D. Wang, B. Ye, W.J. Ding, Nanoparticle-inhibited growth of primary aluminum in Al-10Si alloys, *Acta Mater.* 103 (2016) 252–263.
- [60] N.C. Verissimo, C. Brito, W.L.R. Santos, N. Cheung, J.E. Spinelli, A. Garcia, Interconnection of Zn content, macrosegregation, dendritic growth, nature of intermetallics and hardness in directionally solidified Mg-Zn alloys, *J. Alloy. Comp.* 662 (2016) 1–10.